A&A 533, A12 (2011)
DOI: 10.1051/0004-6361/201117121
© ESO 2011

Astronomy & Astrophysics

Benchmarking atomic data for astrophysics: Fe XIII EUV lines

G. Del Zanna

Department of Applied Mathematics and Theoretical Physics, University of Cambridge, Wilberforce road, Cambridge CB3 0WA, UK
e-mail: G.Del-Zanna@damtp.cam.ac.uk

Received 20 April 2011 / Accepted 13 July 2011

ABSTRACT

Recent atomic data for Fe XIII are benchmarked against high-resolution spectroscopic observations of the solar corona. All the identifications of the EUV lines are reviewed by also taking into account laboratory measurements. A few new identifications are proposed, and many wavelengths are revised. All the strongest EUV lines are now identified. Very good agreement between predicted and observed line intensities is generally found using the latest atomic calculations. We clearly indicate which EUV lines are blended, and which are best for electron-density measurements in different regimes.

Key words. atomic data – line: identification – techniques: spectroscopic – Sun: corona

1. Introduction

This paper is one in a series (see Del Zanna et al. 2004, hereafter Paper I) that aims to provide an assessment of atomic data needed for the analysis of astrophysical spectra by benchmarking them against all available experimental data. The approach is observation-based, i.e. focuses on the brightest spectral lines that are observed in solar and/or laboratory spectra.

Fe XIII is an important ion for the solar corona (in particular active regions) because it produces strong EUV spectral lines, which are routinely used to measure electron densities using data from e.g. the SOHO Coronal Diagnostic Spectrometer (CDS, see Harrison et al. 1995) and especially the Hinode EUV Imaging Spectrometer (EIS, see Culhane et al. 2007). This latter instrument is more sensitive than CDS and has a higher spectral resolution, so accurate densities can be obtained (see e.g., Watanabe et al. 2009; Young et al. 2009).

Compared to other Fe ions, the atomic data for Fe XIII have been quite good. The energies of most of the lower levels of the $3s^2\,3p^2$, $3s\,3p^3$, $3s^2\,3p\,3d$, and $3s\,3p^3$ are known, and various atomic calculations for electron impact excitation have been published. The most recent ones are from Gupta & Tayal (1998, hereafter GT98), Aggarwal & Keenan (2005, hereafter AK05), and Storey & Zeippen (2010, hereafter SZ10), all of which employed the accurate R-matrix method. Various shortcomings in the calculations made by AK05 and GT98 were pointed out by SZ10, however. All these calculations have been benchmarked against the best observations. Keenan et al. (2007) did report some comparisons between observed intensities and those predicted with the AK05 atomic data, however considerable discrepancies in a number of cases were found. Section 2 briefly describes the experimental data considered for this benchmark. Section 3 outlines the benchmark method. Section 4 presents a summary of the main results. Section 5 draws the conclusions.

2. Experimental data

Most Fe XIII line identifications in the EUV have been made using laboratory measurements of Fawcett and the group at the Culham laboratories in the sixties and seventies. Prominent papers where most line identifications were obtained are Fawcett et al. (1967), Fawcett (1971), and Bromage et al. (1978). Some of the original plates and unpublished material obtained from Fawcett were used for the present assessment. More recently, a few papers based on laboratory spectroscopy (e.g. beam-foil and electron-beam ion traps) have produced very useful spectral data. A number of new identifications were proposed by Jupen et al. (1993, hereafter J93), some based on previous laboratory work by Träbert.

2.1. Solar EUV spectra

Behring et al. (1976) published a line list based on an LASP rocket flight that observed the entire Sun in the 60–385 Å region. That spectrum is still the best in terms of resolution (0.06 Å) and wavelength accuracy (few mÅ). In terms of radiometric calibration, the best EUV spectrum is still the one recorded at 50–300 Å by a grazing-incidence spectrometer flown on a rocket in 1969 (Malinovsky & Heroux 1973). At longer wavelengths, the best active region spectrum is the one obtained by the Goddard Solar Extreme Ultraviolet Rocket Telescope and Spectrograph flown in 1989 (SERTS-89) (Thomas & Neupert 1994, hereafter TN94), which observed the 235–450 Å range in first order. The SERTS-97 (Brosius et al. 2000) covered the 300–353 Å spectral region. Both SERTS-89 and SERTS-97 were radiometrically calibrated. The SERTS-95 spectra (Brosius et al. 1998b), used by Keenan et al. (2007) in their benchmark, covered the 171–225 Å band in second order, and the 235–335 Å region in first order with excellent spectral resolution (similar to Behring et al. 1976). However, older atomic data (CHIANTI version 1.01) were actually used by Brosius et al. (1998a) to calibrate the SERTS-95 spectra. The comparison between observations and theory is for most lines not as good as what is obtained with Hinode/EIS. The rocket employed a multilayer grating that enhanced the sensitivity in the second order. Multi-layers have a sharply-peaked response and it is possible that the discrepancies are caused by the calibration, which is in need of improvement.

The ESA/NASA Solar and Heliospheric Observatory (SOHO) has produced a wealth of spectral data with the CDS and SUMER instruments. The CDS covers a wide wavelength range (150–780 Å) at medium resolution (0.3 Å) with nine

channels, distributed between a normal incidence (NIS) and a grazing incidence (GIS) spectrometer. Data from CDS as described in Del Zanna (1999) were used for the benchmark, but the results are very similar to those obtained with the SERTS rockets, so they will not be shown here.

The Hinode/EIS instrument covers two EUV wavelength bands (SW: 166–212 Å; LW: 245–291 Å). A complex data processing, which included various geometrical corrections and a wavelength calibration procedure, was applied to the data, as described in detail in Del Zanna (2009b). The main correction was for the slant in the SW and LW spectra, to ensure that different spectral regions were co-spatial (see Del Zanna & Ishikawa 2009). For the present benchmark we have used a large number of Hinode/EIS observations, but we present here results from only one, on 2007 May 21. This observation and the analysis of the data is described in Del Zanna & Ishikawa (2009). A high-density "moss" region with strong Fe XIII lines was selected, and an averaged spectrum obtained (to increase the S/N). Line radiances were obtained with the Lang et al. (2006) effective areas and a CCD gain of 6.3. The wavelengths of the strongest lines are within 5 mÅ of the Behring et al. (1976) values, which makes this the typical uncertainty in the EIS measurements.

3. Atomic data and benchmark method

The present paper is focused on the three main $n = 3$ spectroscopic configurations in Fe XIII, $3s^2\ 3p^2$, $3s\ 3p^3$, and $3s^2\ 3p\ 3d$ that produce 27 fine-structure levels and all the brightest lines for this ion. Additional levels from the $3p^4$ and $3s\ 3p^2\ 3d$ configurations are also discussed below.

Many atomic structure calculations for Fe XIII have been published, the most notable one being the relativistic multireference many-body perturbation theory calculation of Vilkas & Ishikawa (2004), because it provides energies very close to the experimental ones. These authors calculated only the energies of the lowest 27 levels arising from the $3s^2\ 3p^2$, $3s\ 3p^3$, and $3s^2 3p\ 3d$ configurations.

Gupta & Tayal (1998) published only effective collision strengths for a limited number of transitions arising form the $3s^2\ 3p^2$, $3s\ 3p^3$, and $3s^2 3p\ 3d$ configurations. These data were complemented with A-values calculated for CHIANTI by Young (2004) using the SUPERSTRUCTURE programme (Eissner et al. 1974). This model ion is what has been available within CHIANTI (Dere et al. 1997) since version 4 (Young et al. 2003) in 2003 and is adopted here.

Aggarwal & Keenan (2005) calculated effective collision strengths and A-values for transitions arising from the $3s^2\ 3p^2$, $3s\ 3p^3$, $3s^2 3p\ 3d$, $3p^4$, $3s\ 3p^2\ 3d$, and $3s^2\ 3d^2$ configurations. A model ion has been built using the published data. Notice that the ordering of the levels in AK05 is different from that of the other authors.

Storey & Zeippen (2010) performed an extensive benchmark calculation using SUPERSTRUCTURE, which was used to validate the target for the scattering calculation. The target included terms arising from the $3s^2\ 3p^2$, $3s\ 3p^3$, $3s^2 3p\ 3d$, $3p^4$, $3s\ 3p^2\ 3d$, $3s^2\ 3d^2$, and $3p^3\ 3d$ configurations. For the lowest 27 levels, SZ10 calculated A-values using the more extensive benchmark calculation, the term-energy-correction (TEC) procedure (see, e.g. Zeippen et al. 1977; Nussbaumer & Storey 1978) and observed energies (see their Table 8). They are adopted here, because they are in principle more accurate, but also because they better agree with the observations.

In order to build a complete atomic model for this ion, A-values for all the other transitions have been calculated here with AUTOSTRUCTURE (Badnell 1997), using the same target as in SZ10 (to avoid incorrect assignments of levels), but applying observed energies whenever available. The ordering of a few levels (16, 17, 24, 25) has been modified as in SZ10 to follow the observed level ordering. The present A-values, together with the rates from SZ10 are referred to below as the present atomic model.

The stationary level populations have been solved to obtain $N_j(N_e, T_e)$, the population of level j relative to the total number density of the ion as a function of the electron density and temperature. The line intensities, I_{th}, proportional to $N_j A_{ji}$, are then directly obtained by knowing A_{ji}, the transition probability from the upper level j to the lower level i. The identifications of the brightest lines are then considered by comparing the "emissivity ratios":

$$F_{ji} = \frac{I_{ob}\ N_e\ C}{N_j(N_e, T_0)\ A_{ji}} \tag{1}$$

calculated at a fixed temperature $\log T_0\ [K] = 6.2$ and plotted as a function of the electron density N_e. There are some temperature effects for this ion, but they are small and are not discussed here. I_{ob} is the observed intensity in the line. The scaling constant C is chosen so that the curves are close to unity and it is easier to see how good the agreement is. For each dataset/plot a single constant, the same for all the lines, is chosen. If theory and observations agree, all F_{ji} curves will either overlap or cross at one density value for isodensity and isothermal plasmas. Departures from the isodensity or isothermal case are normally second-order effects, compared to other effects such as line blending and instrument calibration. Temperature effects become important when lines observed at very different wavelengths are compared, because of the different excitation energies, which lead to different emissivities. However, for the comparisons presented here, they are within 10–20% at most.

The identification process for the lines observed by Hinode/EIS was aided by inspecting the integrated intensities over solar active regions and comparing them with those of other lines. This is a powerful method to assess if/where lines are blended.

4. Summary of results

Table 1 lists the energies and identifications of the lowest 27 levels together with the few identified in the other configurations. The experimental level energies E_{exp} (cm^{-1}) together with those from the National Institute of Standards and Technology (NIST) version 3 database[1] are displayed. All 27 levels are now finally firmly established (the full dataset of energies and A-values is made available within CHIANTI v.7, Landi et al. 2011).

Table 2 lists the brightest lines (in decreasing order of intensity), grouped into two wavelength ranges, EUV, and visible/infrared. The wavelengths λ_{exp} corresponding to the experimental energies E_{exp} are shown, as are the wavelengths from the NIST energies λ_{NIST}. For most cases, the NIST wavelengths are close to λ_{exp}, although some differences become significant when high-resolution observations such as those from Hinode/EIS are considered.

It is very satisfactory to see that all the brightest transitions have finally been identified. Intensities were calculated at low (10^8 cm^{-3}) and high (10^{12} cm^{-3}) densities, typical of the quiet-Sun corona and of laboratory spectra. Notice the striking difference in the relative intensities of some lines at different densities.

[1] http://physics.nist.gov

Table 1. Level energies for Fe XIII.

i	Conf.	Lev.	E_{exp}	E_{NIST}
1	$3s^2\ 3p^2$	$^3P_0$	0.0	0.0 (0)
2	$3s^2\ 3p^2$	$^3P_1$	9303.1	9302.5 (1)
3	$3s^2\ 3p^2$	$^3P_2$	18 561.7	18 561.0 (1)
4	$3s^2\ 3p^2$	$^1D_2$	48 069.7	48 068.0 (2)
5	$3s^2\ 3p^2$	$^1S_0$	91 511.0	91 508.0 (3)
6	$3s\ 3p^3$	$^5S_2$	214 624.0	214 608.0 (16)
7	$3s\ 3p^3$	$^3D_1$	287 205.0	287 205.0 (0)
8	$3s\ 3p^3$	$^3D_2$	287 356.0	287 360.0 (–4)
9	$3s\ 3p^3$	$^3D_3$	290 180.0	290 210.0 (–30)
10	$3s\ 3p^3$	$^3P_0$	328 927.0	–
11	$3s\ 3p^3$	$^3P_1$	329 637.0	329 647.0 (–10)
12	$3s\ 3p^3$	$^3P_2$	330 282.0	330 279.0 (3)
13	$3s\ 3p^3$	$^1D_2$	362 407.0	362 330.0 (77)
14	$3s\ 3p^3$	$^3S_1$	415 462.0	415 462.0 (0)
15	$3s^2\ 3p\ 3d$	$^3F_2$	430 124.0	–
16	$3s\ 3p^3$	$^1P_1$	438 086.0	438 050.0 (36)
17	$3s^2\ 3p\ 3d$	$^3F_3$	436 919.0	–
18	$3s^2\ 3p\ 3d$	$^3F_4$	447 001.0	–
19	$3s^2\ 3p\ 3d$	$^3P_2$	486 358.0	486 358.0 (0)
20	$3s^2\ 3p\ 3d$	$^3P_1$	494 942.0	494 942.0 (0)
21	$3s^2\ 3p\ 3d$	$^1D_2$	498 870.0	498 870.0 (0)
22	$3s^2\ 3p\ 3d$	$^3P_0$	501 514.0	503 340.0 (–1826)
23	$3s^2\ 3p\ 3d$	$^3D_1$	506 505.0	506 502.0 (3)
24	$3s^2\ 3p\ 3d$	$^3D_3$	509 176.0	509 176.0 (0)
25	$3s^2\ 3p\ 3d$	$^3D_2$	509 250.0	509 250.0 (0)
26	$3s^2\ 3p\ 3d$	$^1F_3$	556 911.0	556 870.0 (41)
27	$3s^2\ 3p\ 3d$	$^1P_1$	570 743.0	570 690.0 (53)
28	$3p^4$	$^3P_2$	591 362.0	–
42	$3s\ 3p^2\ 3d$	$^3F_2$	669 564.0	–
56	$3s\ 3p^2\ 3d$	$^3D_2$	753 767.0	–
60	$3s\ 3p^2\ 3d$	$^3F_2$	777 950.0	–
61	$3s\ 3p^2\ 3d$	$^3F_3$	783 540.0	–
64	$3s\ 3p^2\ 3d$	$^3F_4$	792 105.0	–
72	$3s\ 3p^2\ 3d$	$^3D_2$	817 170.0	–
84	$3s\ 3p^2\ 3d$	$^3P_2$	897 511.0	–

Notes. Columns indicate the indices, the configuration, the dominant *LSJ*, the experimental level energies E_{exp} (cm^{-1}), and those from NIST. Values in parentheses indicate differences with the experimental energies. Only a selection of observed levels from the lower configurations that produce the EUV lines discussed here are presented.

The benchmark and identification of the lines was made by determining which line should be well observable in the different density regimes. For example, the decays to excited states are strong in high-density spectra such as those of the theta-pinch device taken by Fawcett and some become visible in the active region spectra of the Sun.

Figure 1 shows the emissivity ratio curves for the main lines observed by Malinovsky & Heroux (1973) using the atomic data from GT98, AK05, and SZ10. There are clear discrepancies with the AK05 data, but a good agreement is found with both the GT98 and SZ10 data, with typical quiet Sun densities obtained. The disagreements when using the AK05 data extend to other cases, but they are not shown here. Partly as a consequence of this, many of the results and new identifications discussed in Keenan et al. (2007) turn out to be incorrect.

Figure 2 shows the emissivity ratios obtained from the high-density Hinode/EIS spectrum and the GT98 and SZ10 atomic data, with the same selection of strong lines as in Fig. 1. There clearly is a problem in the predicted intensities of the decays from level 23 in the GT98 data. This is not present in the

Table 2. List of the brightest Fe XIII lines, from the EUV to the visible.

$i-j$	Int 1×10^8	Int 1×10^{12}	λ_{exp} (Å)	λ_{NIST} (Å)	
1–20	1.0	0.12	202.044	202.044	
3–14	0.26	0.19	251.952	251.952	
2–23	0.20	0.10	201.126	201.127	
3–20	0.15	1.8×10^{-2}	209.916	209.916	
2–14	0.13	9.8×10^{-2}	246.209	246.209	
3–24	7.4×10^{-2}	0.39	203.826	203.826	sbl
3–23	6.3×10^{-2}	3.2×10^{-2}	204.942	204.943	
1–14	5.4×10^{-2}	3.9×10^{-2}	240.696	240.696	bl
1–23	4.0×10^{-2}	2.1×10^{-2}	197.431	197.433	
3–25	3.4×10^{-2}	0.14	203.795	203.795	sbl
7–60	3.0×10^{-2}	4.3×10^{-3}	203.772	–	N sbl
3–17	3.3×10^{-2}	3.4×10^{-2}	239.030	–	N
4–16	3.6×10^{-2}	0.13	256.400	256.422	R bl
2–25	2.4×10^{-2}	9.9×10^{-2}	200.021	200.021	
4–15	2.7×10^{-2}	1.4×10^{-2}	261.743	–	N
4–21	2.1×10^{-2}	0.15	221.828	221.827	
2–19	1.8×10^{-2}	8.6×10^{-2}	209.619	209.619	
8–60	1.8×10^{-2}	2.5×10^{-3}	203.835	–	N sbl
3–19	1.8×10^{-2}	8.7×10^{-2}	213.768	213.768	
4–20	1.7×10^{-2}	2.0×10^{-3}	223.778	223.777	
4–19	1.6×10^{-2}	7.6×10^{-2}	228.160	228.159	
2–22	1.4×10^{-2}	4.0×10^{-2}	203.165	202.414	N
2–21	1.2×10^{-2}	8.6×10^{-2}	204.262	204.262	
8–56	1.2×10^{-2}	2.4×10^{-3}	214.403	–	N
3–15	1.2×10^{-2}	6.2×10^{-3}	242.977	–	N
4–26	7.5×10^{-3}	0.25	196.525	196.540	R bl
2–15	8.8×10^{-3}	4.7×10^{-3}	237.631	–	N
5–27	6.9×10^{-3}	6.8×10^{-2}	208.667	208.689	R bl
4–23	7.0×10^{-3}	3.6×10^{-3}	218.133	218.134	
4–25	6.8×10^{-3}	2.8×10^{-2}	216.835	216.834	
14–84	5.9×10^{-3}	3.1×10^{-3}	207.448	–	N bl
2–20	5.8×10^{-3}	6.8×10^{-4}	205.914	205.914	
2–16	6.3×10^{-3}	2.4×10^{-2}	233.218	233.238	R
15–60	6.5×10^{-3}	9.3×10^{-4}	287.500	–	TN
17–72	5.7×10^{-3}	2.0×10^{-3}	262.984	–	TN
4–14	5.1×10^{-3}	3.7×10^{-3}	272.189	272.187	
5–16	5.1×10^{-3}	1.9×10^{-2}	288.538	288.565	R
4–24	2.8×10^{-3}	1.4×10^{-2}	216.870	216.869	
8–61	2.4×10^{-3}	7.5×10^{-3}	201.538	–	N bl
9–64	1.9×10^{-3}	1.5×10^{-2}	199.233	–	N
3–26	3.8×10^{-4}	1.3×10^{-2}	185.753	185.767	R
1–7	0.27	4.8×10^{-2}	348.183	348.183	
2–11	9.1×10^{-2}	3.3×10^{-2}	312.174	312.164	R
2–8	9.1×10^{-2}	0.10	359.644	359.638	
1–11	6.0×10^{-2}	2.2×10^{-2}	303.364	303.355	R bl
2–7	7.0×10^{-2}	1.2×10^{-2}	359.839	359.838	
3–9	6.2×10^{-2}	0.15	368.164	368.122	R
3–11	4.4×10^{-2}	1.6×10^{-2}	321.466	321.455	R
3–12	3.7×10^{-2}	0.11	320.800	320.803	bl
4–13	2.1×10^{-2}	0.13	318.130	318.206	R bl
9–28	1.5×10^{-2}	6.2×10^{-3}	332.025	–	TN
15–42	1.5×10^{-2}	3.2×10^{-3}	417.641	–	TN
2–10	9.7×10^{-3}	2.4×10^{-2}	312.868	–	
2–6	1.2×10^{-2}	8.9×10^{-3}	487.042	487.079	
2–12	4.7×10^{-3}	1.4×10^{-2}	311.547	311.549	bl
4–9	4.6×10^{-3}	1.1×10^{-2}	413.035	412.981	
5–14	3.3×10^{-3}	2.4×10^{-3}	308.689	308.686	

Table 2. continued.

$i-j$	Int 1×10^{8}	Int 1×10^{12}	λ_{exp} (Å)	λ_{NIST} (Å)
3–8	3.0×10^{-3}	3.4×10^{-3}	372.032	372.025
3–6	1.9×10^{-2}	1.5×10^{-2}	510.042	510.082
1–2	2.0	5.7×10^{-4}	10 749.11	10 749.80
2–3	1.1	6.5×10^{-4}	10 800.77	10 800.89
2–4	0.14	3.3×10^{-3}	2579.54	2579.61
3–4	0.17	4.0×10^{-3}	3388.91	3389.03
2–5	4.4×10^{-2}	6.1×10^{-3}	1216.43	1216.46

Notes. The lines are grouped into two wavelength ranges, EUV and visible/infrared, and are displayed in decreasing order of intensity. Columns 2, and 3 show the relative line intensities (photons) Int = $N_j A_{ji}/N_e$ calculated at log T[K] = 6.2 and electron densities of 10^8, 10^{12} cm^{-3}, normalized to the intensity of the brightest EUV line at 10^8 cm^{-3}. The last columns show the wavelengths corresponding to the experimental energies E_{exp} of Table 1, and those from the NIST energies. N indicates a new identification, TN a new tentative one, and R a revised wavelength. bl indicates a blend, sbl a self-blend.

SZ10 data, although the decay to the ground state is over-predicted theoretically, i.e. cannot be explained with the presence of a blend (see discussion below).

Another problem worth mentioning here is that the two decays from level 14 have observed intensities that are clearly a factor of two too low. This is independent of the atomic data used, and cannot be an atomic physics problem because the well-calibrated Malinovsky & Heroux (1973) spectrum shows excellent agreement. A similar problem (of a factor of two) was found around 255 Å by Del Zanna & Ishikawa (2009), and points to a radiometric calibration problem in the Hinode/EIS LW channel.

Figure 3 shows the emissivity ratio curves for the remainder of the lines observed with Hinode/EIS, and the SZ10 atomic data. Many lines are new identifications, as described below.

Figure 4 shows the emissivity ratio curves obtained from the Behring et al. (1976) spectrum and the SZ10 data. The spectrum was not radiometrically calibrated, but the emissivity ratios show that a calibration of Behring et al. (1976) is not really needed when lines close in wavelength are considered. Indeed, the lines which agree well in the Malinovsky & Heroux (1973) and EIS spectra also agree well in the Behring et al. (1976) spectrum. The great advantage of the Behring et al. (1976) spectrum is its superior spectral resolution, which allows to benchmark lines that are clearly blended even in the high-resolution Hinode/EIS spectrum.

Figure 5 displays the emissivity ratio curves for the SERTS-89 and SERTS-97 calibrated spectra with the SZ10 atomic data. A discussion on the levels and transitions is given below.

4.1. The ground configuration $3s^2\ 3p^2$

The famous 1–2 and 2–3 infrared transitions were measured in air by Penn & Kuhn (1994) at 10746.17 ± 0.005 and 10797.83 ± 0.005, providing energies of 9303.1 and 18561.7 cm^{-1} for the $^3P_{1,2}$ levels, adopting the standard formula for the refractive index of air given by Edlén (1966).

The energy of the $^1D_2$ (No. 4) is obtained from the 2–4 transition observed by Sandlin et al. (1977) at 2578.77 ± 0.01 Å in air, giving 48069.7 cm^{-1}. More recently, Schmitt & Wichmann (2001) have observed for the first time the 3–4 visible transition at 3387.96 Å from a ground-based spectrum of CN Leo.

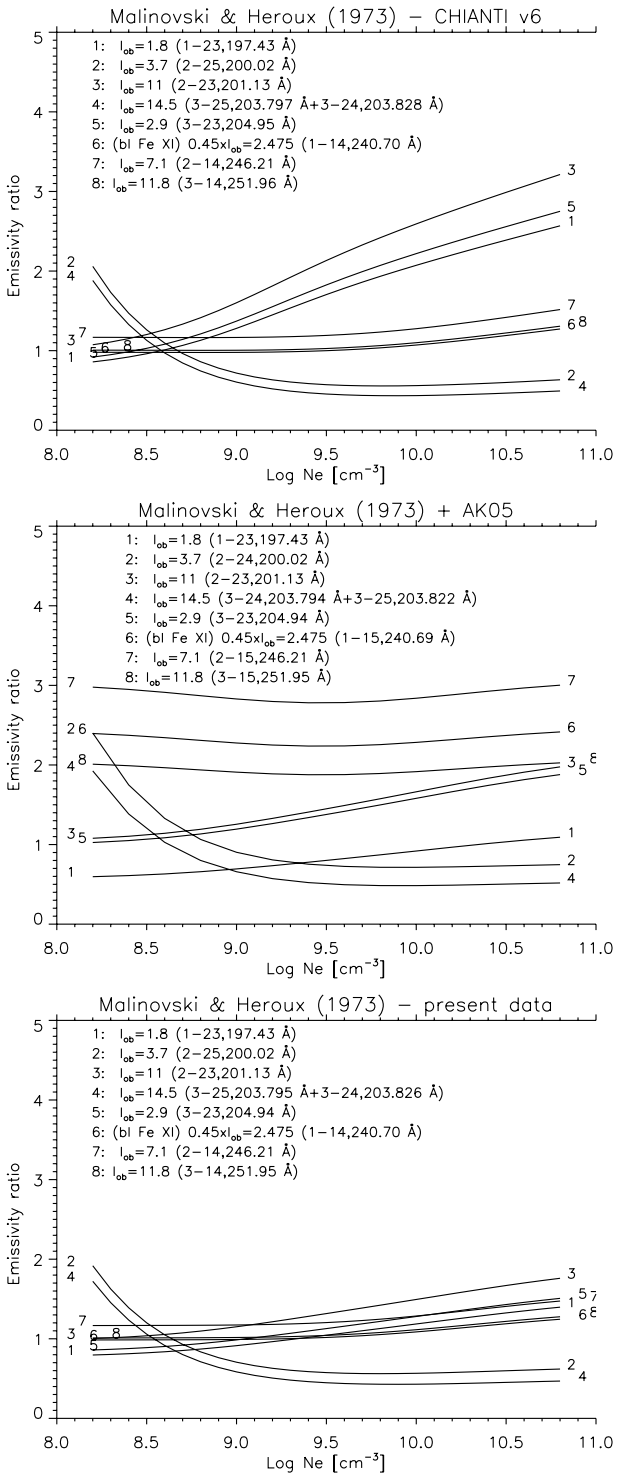

Fig. 1. Emissivity ratio curves relative to the full-Sun spectrum of Malinovsky & Heroux (1973), and the atomic data from GT98, AK05 and SZ10. I_{ob} indicates the observed irradiances (10^{-3} erg cm^{-2} s^{-1}). The indices of the lower and upper levels as in Table 1 and the present experimental wavelengths (Table 2) are also shown.

When converted to vacuum, this latter measurement provides 48069.5 cm^{-1}, which agrees very well. The $^1S_0$ level (No. 5) has had various energies assigned in the past, owing to differing identifications of the 2–5 transition, which was originally suggested as being the 1213.0 Å coronal line (that actually is a strong S x transition). The last currently accepted one was

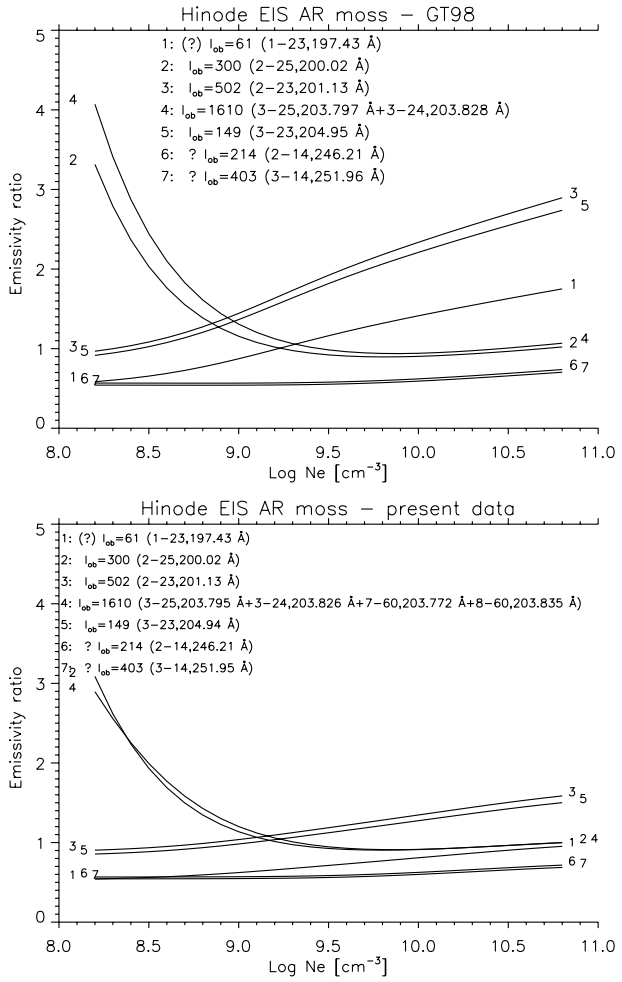

Fig. 2. Emissivity ratio curves for a selection of strong lines observed with Hinode/EIS. The *upper* plot is obtained with the GT98 atomic data, and the *lower* one with the SZ10 ones. Intensities are given in phot cm^{-2} s^{-1} sr^{-1}.

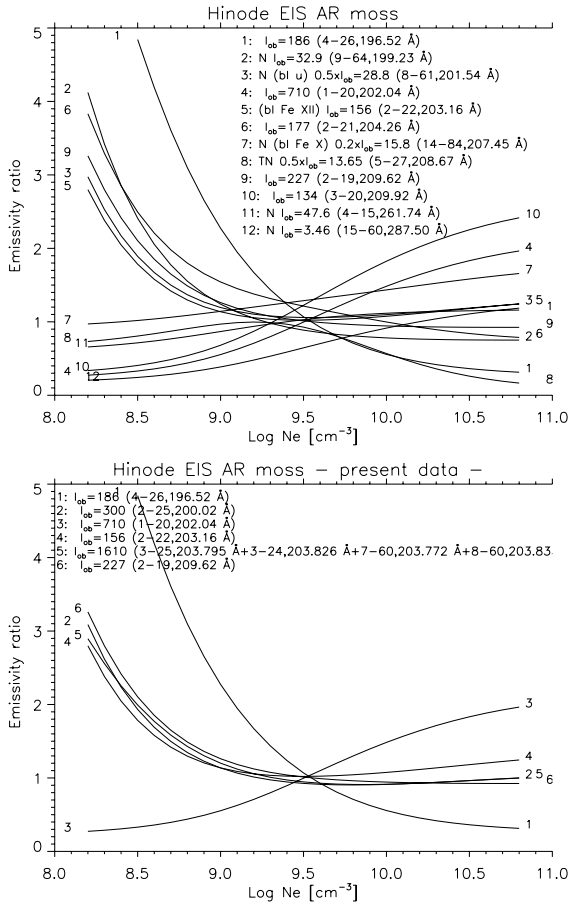

Fig. 3. Emissivity ratio curves for a selection of lines observed with Hinode/EIS, and the SZ10 atomic data. N indicates a new identification, TN a tentative one. The *upper* plot shows the weaker lines, and the *lower* the strongest and most reliable lines to measure densities.

suggested by Sandlin in 1975 (see Doschek et al. 1976) and measured by Sandlin et al. (1977) at 1216.43 ± 0.01 Å, providing 91 511 cm^{-1}. The line is difficult to observe because of its proximity to the hydrogen Ly α. J93 identified the 2–16 and 5–16 transitions with lines observed at 233.218 and 288.577 Å respectively, which would provide an energy for level 5 of 91 558 cm^{-1}. The J93 measurements are well outside the uncertainty provided by the Sandlin et al. (1977) wavelength. Preference is given to the more direct measurement from Sandlin et al. (1977).

4.2. The 3s 3p^3 configuration

The $^5S_2$ level (No. 6) produces two observable EUV transitions, 2–6 and 3–6. Following their original identification in beam-foil spectra by Träbert et al. (1987), J93 measured them at 487.042 and 510.042 Å. We have found no solar observations of these lines yet. This level is the only one for which the AUTOSTRUCTURE energy is very different, so alternative identifications (e.g. in SOHO/CDS and SUMER spectra) were sought without success. It should be noted, however, that the wavelength difference of these two lines exactly agrees with the energies of levels 2, 3 (providing an energy for the $^5S_2$ of 214 624 cm^{-1}), and that the ab-initio energy calculated by Vilkas & Ishikawa (2004) is very close (214 540 cm^{-1}).

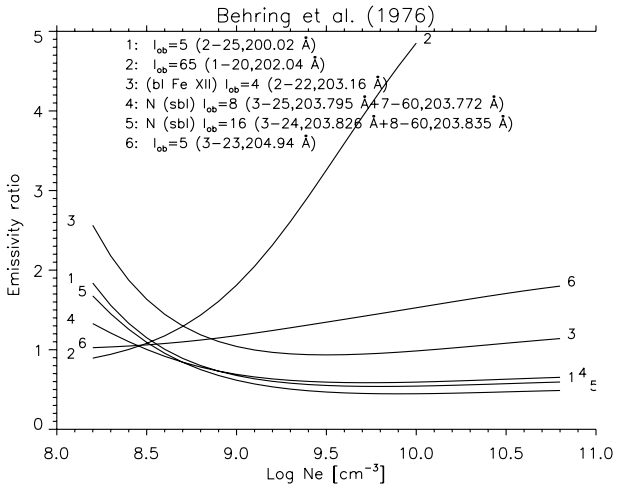

Fig. 4. Emissivity ratio curves for a selection of lines relative to the full-Sun Behring et al. (1976) spectrum.

The energy of level 7 ($^3D_1$) is obtained from the 1–7 and 2–7 lines observed by TN94 at 348.182 ± 0.001 and 359.830 ± 0.004 Å. The energy of level 8 ($^3D_2$) is obtained from the 2–8 line observed at 359.638 ± 0.01 by Be76. The 359.638 and

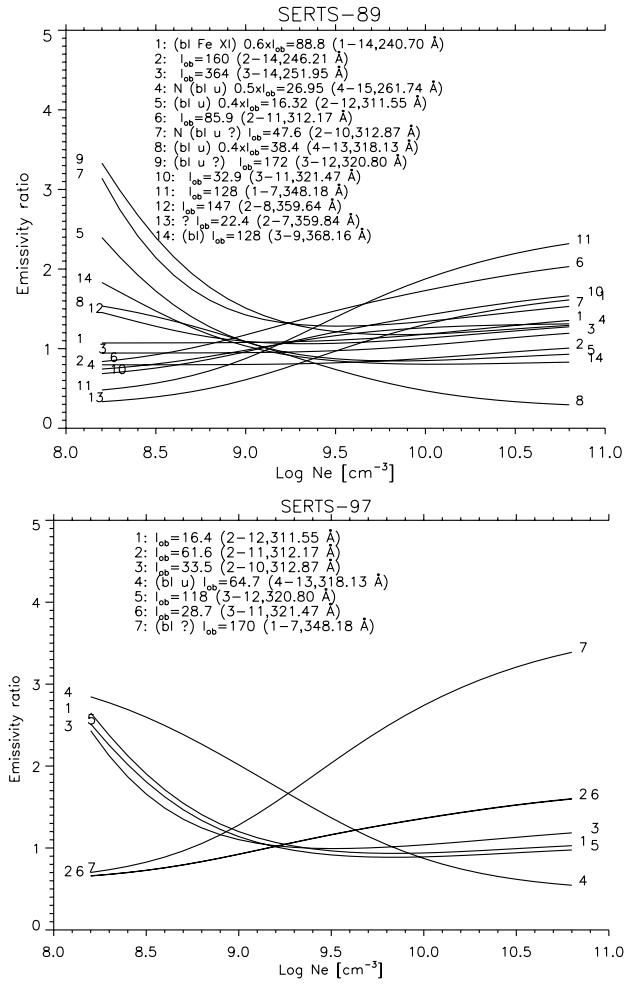

Fig. 5. Emissivity ratio curves for the SERTS-89 and SERTS-97 calibrated data. Intensities are in erg cm^{-2} s^{-1} sr^{-1}.

359.830 Å transitions are blended in most spectra, but they are still a good density diagnostic when measured in conjunction with the 348.182 Å line.

Level 9 (^{3}D$_3$) produces two observable transitions, 3–9 and 4–9. The 3–9 transition was listed as unidentified in the TN94 spectrum, but its intensity agrees well with the predicted one, as Fig. 5 shows. We adopt the TN94 368.163 Å wavelength to obtain an energy for the ^{3}D$_3$ level of 290 180 cm^{-1}. In most spectra, this transition is blended with the strong Mg IX resonance line at 368 Å. The weaker 4–9 line was observed by TN94 at 412.997 and by J93 at 413.044 Å (which provides an energy of 290 175 cm^{-1}).

The energy of level 10 (^{3}P$_0$) is from the 2–10 transition, listed as unidentified by TN94 and observed at 312.868 Å. This transition was identified by J93 with a laboratory 312.88 Å line.

The energy of level 11 (^{3}P$_1$) is from the 2–11 transition, first identified by Be76 with a line at 312.164 ± 0.004 Å. The emissivity ratios show that this line has the right intensity. However, TN94 observed the line at 312.174 ± 0.002 Å, also with the correct intensity (see Fig. 5). Jupen et al. (1993) did not observe this line in their tokamak spectra, and identified it with a line at 312.095 ± 0.008 Å. The latter identification has to be rejected, but the difference in the Be76 and TN94 wavelengths is puzzling. The TN94 measurement is chosen, given the fact that the line is strong in their active region spectrum. This predicts that the decay of the ^{3}P$_1$ to the ground state should be at 303.364 Å, i.e. the line is blended with the much stronger Si XI 303.325 Å resonance line.

The energy of level 12 (^{3}P$_2$) is from the 3–12 transition, first identified by Be76 and measured by TN94 and Be76 at 320.800 ± 0.002 Å. The decay to the first excited state is observed at 311.555 Å but is clearly blended with an unidentified line (see Fig. 5). The energy of level 13 (^{1}D$_2$) is obtained here from the 4–13 transition, observed by Be76 and TN94 at 318.14 and 318.12 Å, respectively. This line is not blended in the Be76 quiet Sun but it is blended in active region spectra (see Fig. 5).

The energy of level 14 (^{3}S$_1$) is from the very strong 3–14, 2–14 transitions, observed at 251.953 and 246.208 Å by Be76. The decay to the ground state is observed at 240.713 Å but is clearly blended with Fe XI as discussed in Del Zanna (2010).

The energy of level 16 (^{1}P$_1$) is obtained from the weak 2–16 transition observed by J93 at 233.218 ± 0.008 Å (Be76 observed the line at 233.234 ± 0.01 Å). This predicts that the strong 4–16 line should have a wavelength of 256.400 Å. This line is blended with a strong Si X line (256.38 Å).

4.3. The 3s^2 3p 3d configuration

For details about the identification of the ^{3}F$_{2,3,4}$ levels see J93, Vilkas & Ishikawa (2004), and Träbert et al. (2011). The present model predicts that the strongest line is the 4–15 transition, observed with Hinode/EIS at 261.743 Å, and with excellent agreement between observed and predicted intensity (see Fig. 3).

The energy of level 19 (^{3}P$_2$) is obtained from the 2–19 and 3–19 transitions, observed by Be76 at 209.617 and 213.770 Å, respectively. The 4–19 line is blended with S X 228.167 Å. The ^{3}P$_1$ (level 20) produces the strongest EUV line with a decay to the ground state observed at 202.044 ± 0.002 Å by Be76. The ^{1}D$_2$ is known from the 2–21 transition, observed by Be76 at 204.263 ± 0.01 Å, and by Hinode/EIS at 204.257 ± 0.005 Å.

Level 22 (^{3}P$_0$) produces a well observable line (2–22). J93 identified it with a tokamak line observed at 203.152 ± 0.008 Å. Be76 observed a weak line at 203.173 ± 0.01 Å, which appears to be blended in their quiet Sun spectrum (see Fig. 4). In active region spectra, Hinode/EIS observes a strong line at 203.165 ± 0.005 Å with exactly the expected intensity (see Fig. 3), so the EIS measurement is adopted.

Level 23 (^{3}D$_1$) is one of the most complex ones. It produces three strong transitions (2–23, 3–23 and 1–23). For its energy, the 3–23 measurement of 204.942 ± 0.004 Å from Be76 is adopted here. The strong 2–23 line, predicted at 201.126 Å, is listed as blended in Be76. However, its Hinode/EIS intensity agrees relatively well with the predicted one. The same is true for the 3–23 line, but not the decay to the ground. The fact that the intensity of the 1–23 transition observed by Hinode/EIS is too low could be caused by an EIS calibration problem, considering that the Malinovsky & Heroux (1973) spectrum agrees within a relative 20%. However, it is worth pointing out that the *A*-values for the decay branches from this level are very sensitive to the target, and very different line intensities are obtained when different sets of *A*-values are adopted. The present atomic model is the one that reproduces these lines best.

Levels 24 and 25 (^{3}D$_{3,2}$) are particularly important because they produce the strong 3–24 and 3–25 transitions observed by Be76 at 203.826 ± 0.01 Å and 203.793 ± 0.02 Å

respectively, and used extensively to measure electron densities in the solar corona. Behring et al. (1976) clearly separated these two lines which are usually blended in most spectra, including Hinode/EIS. As described below, these two transitions appear to be further blended. The $^3D_2$ also produces a strong, unblended line (2–25) at 200.021 ± 0.004 Å. Its observed intensity agrees well with the predicted one and with the 203.8 Å self-blend, as Figs. 1, 2, 4 show. Either the 200.021 or the 203.8 Å self-blend can be used to measure electron densities only to about $10^{9.5}$ cm^{-3}. Better measurements at higher densities can be obtained from the strong 4–26 transition, observed by Be76 at 196.525 ± 0.01 Å (in good agreement with the Hinode/EIS value of 196.519 ± 0.005 Å).

Level 27 ($^1P_1$) produces the 5–27 transition, expected to be well visible in high-density conditions. Bromage et al. (1978) identified this transition with the weak 208.679 ± 0.01 Å line observed by Be76. Hinode/EIS spectra of active regions show a number of transitions at those wavelengths, most notably at 208.65 and 208.70 Å, but they all appear to be blended, considering their intensities. A wavelength of 208.667 Å from one of Fawcett plates, where this line is very strong, is therefore adopted here.

4.4. The $3p^4$ configuration

Lines from this configuration have not been identified previously. The strongest transitions from this configuration are expected to be the 9–28 and 8–28 transitions. In the active region spectrum of TN94, the present model predicts that the 9–28 line should have an intensity of about 15 (erg cm^{-2} s^{-1} sr^{-1}), while the 8–28 one only about 5, i.e. very weak and not observable. The previous level (27) from the $3s^2$ 3p 3d configuration has a difference between experimental and ab-initio AUTOSTRUCTURE energy of 11 000 cm^{-1}. A similar energy difference for the $3p^4$ predicts that the 9–28 transition should fall around 332 Å. In the TN94 spectrum there are various lines around 332 Å, but the only one that has the correct intensity is the 332.049 Å one, which was tentatively identified by TN94 as Cr XII. It is suggested that this could be instead the 9–28 transition. On the other hand, the intensity of this line as observed by SERTS-97 (at 332.26 Å) is a factor of three too low. Alternatives are that the 9–28 transition is the SERTS-97 unidentified line at 330.218 Å (but not observed by TN94), or that it is blended with other strong transitions.

4.5. The 3s $3p^2$ 3d configuration

Lines from this configuration have not been identified previously. Compared to the previous case, there are a few EUV lines that are deemed observable. All possible combinations have been looked at, searching for wavelength coincidences within a range of about 10 Å in each case.

The strongest transitions are the decays from level 60 ($^3F_2$): the 7–60 and 8–60, only about 0.05 Å apart. Their cumulative intensity at low densities is significant, making it the 9th strongest EUV transition for this ion (see Table 2). Assuming an energy difference of 11 000 cm^{-1} places this self-blend around 203 Å. Most of the nearby lines (201.54, 201.734, 202.608, 204.263, 206.169 Å) are excluded because they are too weak. The 200.021, 201.121, and 202.044 Å lines are purely caused by the Fe XIII 2–25, 2–23 and 1–20 transitions as discussed above. The 202.71 Å is excluded because most of its intensity is caused by Fe XI (see Del Zanna 2010). The 203.173 Å was listed as unidentified in Be76, but its intensity is mostly caused by the 2–22 Fe XIII transition (see Fig. 4). The 203.727 Å is mostly caused by Fe XII as shown in Del Zanna & Mason (2005). The 204.942 Å is caused by the Fe XIII 3–23 transition as discussed above. So at the end we are left with only two reasonable options, the 202.424 Å line, listed as unidentified in Be76 but actually about half of its intensity caused by Fe XI (see Del Zanna 2010), or the 203.8 Å self-blend. The former provides an energy difference of 10 576 cm^{-1}, while the second one 14 000 cm^{-1}. There is another much weaker decay from the same level to level 15, which in principle could be used to establish which of the two is the correct identification. The first option predicts a line at 284.69 Å. There is no clear line in the Hinode/EIS spectra (a pseudo-continuum of lines is present). The second case predicts a line at 287.49 Å, and indeed there is a line at exactly the right wavelength. The line is almost within the noise and its observed intensity is very uncertain (within a factor of two of the predicted one, see Fig. 3).

To confirm the identification of level 60 ($^3F_2$) it is therefore necessary to look at the levels 61 and 64 ($^3F_{3,4}$), which produce observable lines: 8–61 and 9–64. The energy separation of the ^3F_j levels is known very accurately, so it is possible to predict where the 8–61 and 9–64 transitions should be. Let us consider the 8–61 first. In the first case, it should be at 200.16 Å. There is indeed a weak line at exactly the same wavelength, but its observed intensity is about a factor of two too weak compared to the prediction. Also, the integrated intensity of this line over active regions, when compared with those of other Fe XIII lines, clearly shows that this line is dominated by cool transition-region emission, with some blending from a coronal line, and consequently it cannot be the 8–61 transition. The second case predicts a line at 201.53 Å. The Hinode/EIS spectra show at least a blend of two lines, one at 201.50 and one at 201.57 Å. The intensity of the 201.50 Å line is more than sufficient to account for the 8–61 transition (see Fig. 3) and shows exactly the same morphology as the other Fe XIII lines.

The 9–64 transition is predicted to be at 197.89 and 199.23 Å for the two cases. There is a line at 197.86 Å but it is an Fe IX transition, as identified by Young (2009) and discussed in Del Zanna (2009a). EIS observes a line at exactly the right wavelength and with exactly the correct intensity at 199.233 Å, as shown in Fig. 3.

It is very unlikely that the various wavelength and intensity combinations are due to mere coincidences, although a firm identification will need new laboratory measurements. It is interesting to note that Be76 do report that the 203.826 ± 0.01 Å is a blend of two lines. Accordingly, it it reasonable to assume that the 7–60 transition is blending the 203.793 Å line, with a wavelength very close to it, and the 8–60 is blending the 203.826 Å one in its red wing. It is difficult to locate the wavelengths of the 7–60 and 8–60 transitions exactly, given the uncertainty in the measurement of the 203.793 Å line. Their wavelengths are chosen to be 203.77 and 203.83 Å. As Fig. 4 shows, the predicted and observed intensities agree very well when the two self-blends are accounted for in the Be76 spectrum. It is worth mentioning here that the presence of these blends only affects the density measurements at low quiet-Sun densities.

After establishing the energies of three levels, we now look for additional identifications. The next strongest line is predicted to be the 7–42 transition. An energy correction of 14 000 cm^{-1} predicts the line to be around 419 Å. In the active region

spectrum of TN94, this line is predicted to have an intensity of about 5 erg cm^{-2} s^{-1} sr^{-1}. The only possibility is that this line is blending one of the observed ones. It is likely that this occurs either for the Fe xv 417.245 Å or the S xiv 417.640 Å. The line is tentatively assigned to the latter, considering that its observed intensity is higher than expected from S xiv.

The next strongest line is the 8–56 transition. An energy correction of 14 000 cm^{-1} predicts the line to be around 214.7 Å. There is indeed a line at 214.405 Å, and is actually the only possibility within a few Å. This line was identified in Del Zanna & Mason (2005) as being caused by only 50% by an Fe xii transition. Assuming that the rest is caused by the 8–56 transition, the observed and predicted intensity excellently agree, as Fig. 3 shows.

The 17–72 transition is weak but well observable by Hinode/EIS, around 262 Å. The line cannot be blending the 261.747 Å line, and other lines are far too weak. This means that the line should be blending either the Si x 261.0 Å or the Fe xvi 263.0 Å. The latter option is tentatively adopted.

5. Summary and conclusions

A comprehensive benchmark of various Fe xiii atomic data against available observations has been presented. All previous EUV line identifications were reviewed by comparing the line intensities calculated with the latest atomic data from Storey & Zeippen (2010), supplemented with *A*-values. The benchmark provides for the first time (cf. Keenan et al. 2007) a remarkable agreement (to within a relative 20% or better) for all the strongest transitions. One exception are the decays from the 3s^2 3p 3d ^{3}D$_1$ level (23), which proved particularly difficult to model. The use of the SZ10 *A*-values improves the comparison, but significant disagreements are still present, so it is recommended that these decays are not used for diagnostic purposes. We also recommend that the Fe xiii lines in the LW channel of Hinode/EIS are not used until the calibration of this channel is understood. The previous atomic calculations from Gupta & Tayal (1998) and Aggarwal & Keenan (2005) do not produce a similar good agreement.

All the strongest transitions for this ion are now identified, and all their wavelengths revised. The assessment also indicated which lines are most likely blended in which solar conditions, and which lines are particularly useful for measuring electron densities. The emissivity ratio plots also clearly indicate in which density regime particular line ratios are better than others. For the Hinode/EIS wavelengths, the best density diagnostics are shown in Fig. 3 (bottom). There is an impressive agreement (to within a relative few percents) between observed and predicted line intensities. Up to about $10^{9.5}$ cm^{-3}, the best diagnostic is the strong self-blend observed at 203.8 Å in conjunction with the only strong decay to the ground state, the 1–20 transition at 202.044 Å. However, that this self-blend appears to be composed of four transitions, and is moreover blended with a strong Fe xii 203.728 Å transition (Del Zanna & Mason 2005) makes the measurement complex. The 2–25 200.02 Å line appears to be an excellent alternative choice together with the weaker 2–19 209.62 Å. Good measurements for high densities can be obtained from the 4–26 196.52 Å line.

Acknowledgements. The support from STFC via the Advanced Fellowship programme and the APAP-Network is acknowledged. P.J. Storey (UCL) is thanked for providing the data and for useful discussions over the past few years. E. Träbert (Bochum and Livermore) is also thanked for useful exchanges of information. B. C. Fawcett is particularly thanked for his continuous encouragement on this long-term benchmark work, a follow-up of his. The anonymous referee is thanked for careful reading and useful comments on the manuscript. Hinode is a Japanese mission developed and launched by ISAS/JAXA, with NAOJ as the domestic partner and NASA and STFC (UK) as international partners. It is operated by these agencies in co-operation with ESA and NSC (Norway). CHIANTI is a collaborative project involving researchers at the Universities of: Cambridge (UK), George Mason, Michigan (USA).

References

Aggarwal, K. M., & Keenan, F. P. 2005, A&A, 429, 1117
Badnell, N. R. 1997, J. Phys. B At. Mol. Phys., 30, 1
Behring, W. E., Cohen, L., Doschek, G. A., & Feldman, U. 1976, ApJ, 203, 521
Bromage, G. E., Fawcett, B. C., Ridgeley, A., & Cowan, R. D. 1978, Opt. Soc. Am. J., 68, 48
Brosius, J. W., Davila, J. M., & Thomas, R. J. 1998a, ApJ, 497, L113
Brosius, J. W., Davila, J. M., & Thomas, R. J. 1998b, ApJS, 119, 255
Brosius, J. W., Thomas, R. J., Davila, J. M., & Landi, E. 2000, ApJ, 543, 1016
Culhane, J. L., Harra, L. K., James, A. M., et al. 2007, Sol. Phys., 60
Del Zanna, G. 1999, Ph.D. Thesis, Univ. of Central Lancashire, UK
Del Zanna, G. 2009a, A&A, 508, 501
Del Zanna, G. 2009b, A&A, 508, 513
Del Zanna, G. 2010, A&A, 514, A41
Del Zanna, G., & Ishikawa, Y. 2009, A&A, 508, 1517
Del Zanna, G., & Mason, H. E. 2005, A&A, 433, 731
Del Zanna, G., Berrington, K. A., & Mason, H. E. 2004, A&A, 422, 731
Dere, K. P., Landi, E., Mason, H. E., Monsignori Fossi, B. C., & Young, P. R. 1997, A&AS, 125, 149
Doschek, G. A., Vanhoosier, M. E., Bartoe, J., & Feldman, U. 1976, ApJS, 31, 417
Edlén, B. 1966, Metrologia, 2, 71
Eissner, W., Jones, M., & Nussbaumer, H. 1974, Comp. Phys. Comm., 8, 270
Fawcett, B. C. 1971, J. Phys. B At. Mol. Phys., 4, 1577
Fawcett, B. C., Gabriel, A. H., & Saunders, P. A. H. 1967, Proc. Phys. Soc., 89, 863
Gupta, G. P., & Tayal, S. S. 1998, ApJ, 506, 464
Harrison, R. A., Sawyer, E. C., Carter, M. K., et al. 1995, Sol. Phys., 162, 233
Jupen, C., Isler, R. C., & Trabert, E. 1993, MNRAS, 264, 627
Keenan, F. P., Jess, D. B., Aggarwal, K. M., et al. 2007, MNRAS, 376, 205
Landi, E., Del Zanna, G., Young, P. R., Dere, K. P., & Mason, H. E. 2011, ApJ, submitted
Lang, J., Kent, B. J., Paustian, W., et al. 2006, Appl. Opt., 45, 8689
Malinovsky, L., & Heroux, M. 1973, ApJ, 181, 1009
Nussbaumer, H., & Storey, P. J. 1978, A&A, 64, 139
Penn, M. J., & Kuhn, J. R. 1994, ApJ, 434, 807
Sandlin, G. D., Brueckner, G. E., & Tousey, R. 1977, ApJ, 214, 898
Schmitt, J. H. M. M., & Wichmann, R. 2001, Nature, 412, 508
Storey, P. J., & Zeippen, C. J. 2010, A&A, 511, A78
Thomas, R. J., & Neupert, W. M. 1994, ApJS, 91, 461
Traebert, E., Hutton, R., & Martinson, I. 1987, MNRAS, 227, 27P
Träbert, E., Ishikawa, Y., Santana, J., & Del Zanna, G. 2011, Can. J. Phys., in press
Vilkas, M. J., & Ishikawa, Y. 2004, J. Phys. B At. Mol. Phys., 37, 1803
Watanabe, T., Hara, H., Yamamoto, N., et al. 2009, ApJ, 692, 1294
Young, P. R. 2004, A&A, 417, 785
Young, P. R. 2009, ApJ, 691, L77
Young, P. R., Del Zanna, G., Landi, E., et al. 2003, ApJS, 144, 135
Young, P. R., Watanabe, T., Hara, H., & Mariska, J. T. 2009, A&A, 495, 587
Zeippen, C. J., Seaton, M. J., & Morton, D. C. 1977, MNRAS, 181, 527